

Theoretical investigation of circular photogalvanic charge currents and linear photogalvanic pure spin currents in HgTe quantum wells

Jun Li,^{1,*} Wen Yang,² Jiang-Tao Liu,^{3,4} Wei Huang,¹ Cheng Li,¹ and Song-Yan Chen¹

¹*Department of Physics, Semiconductor Photonics Research Center, Xiamen University, Xiamen 361005, China*

²*Beijing Computational Science Research Center, Beijing 100089, China*

³*Department of Physics, Nanchang University, Nanchang 330031, China*

⁴*Nanoscale Science and Technology Laboratory, Institute for Advanced Study, Nanchang University, Nanchang 330031, China*

(Dated: October 15, 2018)

Thanks to the strong spin-orbit interaction (SOI), HgTe-based quantum wells (QWs) exhibit very rich spin-related properties. But the full descriptions of them are beyond the simple parabolic band models and conventional Rashba and Dresselhaus SOI terms, as a result of the strong interband coupling of the narrow gap band structures. Here, we develop a theoretical method to calculate the circular photogalvanic effect (CPGE) in Hg_{0.3}Cd_{0.7}Te/HgTe/Hg_{0.3}Cd_{0.7}Te quantum wells (HgTe QWs) based on the realistic eight-band $\mathbf{k} \cdot \mathbf{p}$ model with density matrix formalism. Our method could take account of the unusual band structures and SOIs of HgTe QWs, therefore can be used to calculate the CPGE currents in HgTe QWs with non-parabolic, Dirac-like and inverted energy dispersions. The microscopic origin of CPGE and the interplay effect of structure inversion asymmetry (SIA) and bulk inversion asymmetry (BIA) is also investigated. In addition, this method is extended to study the pure spin currents (PSCs) in HgTe QWs injected by linearly polarized light at normal incidence. Our calculation results support the following findings: (i) In the inverted phase regime, the energy dispersion of heavily inverted HgTe QWs could be strongly distorted, lead to a significant enhancement of CPGE at a certain range of energy spectrum. (ii) The interplay of SIA and BIA could lead to the CPGE currents anisotropically dependent on the azimuth angle of oblique incident light. (iii) The PSC $j_{y'}^{x'}$ ($x' \parallel [110]$ and $y' \parallel [\bar{1}10]$) produced by [110]-linearly-polarized light could change sign with HgTe QW transformed from normal phase to inverted phase. These findings might be utilized in developing the HgTe-based infrared/terahertz optoelectronic and spintronic devices.

PACS numbers: 78.20.Bh, 72.25.Fe, 78.67.De, 71.28.+d, 73.21.Fg

I. INTRODUCTION

HgTe, CdTe and their alloy Hg_{1-x}Cd_xTe ($x \in [0, 1]$) can comprise heterostructures with tunable direct band gap spanning shortwave infrared to terahertz region, and have been mostly developed in the applications of infrared photodetectors [1]. With the rapid growth of spintronics, the spin properties of Hg_{1-x}Cd_xTe systems attracted more and more attentions in recent decades. Many spin-related phenomena have been discovered in these systems, such as the giant [2, 3] and nonlinear spin-splitting [4, 5], the large effective g-factor [6], the intrinsic spin Hall effect [7, 8] and the quantum spin Hall effect [9, 10]. At the heart of these novel phenomena, the very strong spin-orbit interaction (SOI) of Hg_{1-x}Cd_xTe, which inherits from the large relativistic effect of its composing heavy atoms, plays an essential role. Benefiting from the strong SOI, Hg_{1-x}Cd_xTe-based systems have becoming very promising platforms for the explorations of spintronics, topological electronics and the spin-resolved infrared/terahertz optoelectronics [11–14].

To understand the unique spin-related properties of Hg_{1-x}Cd_xTe systems and develop novel devices based on them, the knowledge of SOI in these systems is of great importance. Circular photogalvanic effect (CPGE),

which is identified by the direction change of photocurrents when reversing the helicity of circularly polarized light, has been proved to be an effective approach to study SOIs in semiconductors [15–17]. There are two different kinds of SOI terms responsible for the spin-splittings in low-dimensional semiconductors, i.e., the Rashba SOI (RSOI) term comes from the structure inversion asymmetry (SIA) [18], and the Dresselhaus SOI (DSOI) term originates from the crystal bulk inversion asymmetry (BIA) [19], respectively. CPGE can only be generated in semiconductors lacking inversion symmetries, and is highly sensitive to the spin-splitting of band structure [20]. Therefore the CPGE signals actually carry the symmetry and spin-related information of materials, and have been successfully used as a tool to study the relative ratio of Rashba and Dresselhaus terms (RD ratio) [21, 22]. Recently, the CPGE in Hg_{0.3}Cd_{0.7}Te/HgTe/Hg_{0.3}Cd_{0.7}Te quantum wells (HgTe QWs) has been experimentally observed in terahertz and mid-infrared regions [23, 24]. And this effect was utilized in the fast detection of the infrared-radiation ellipticity [14].

On a macroscopic level, the experimental results of CPGE can be understood by a phenomenological theory without band structure details [17, 23]. Microscopically, the origin of CPGE has been interpreted by parabolic band models with conventional Rashba and Dresselhaus terms [17, 20, 25]. However, these models may not be

* lijun@xmu.edu.cn

implemented in HgTe-based narrow gap quantum wells (QWs), since the band structures of them are very complicated [26, 27] and the spin-splittings are nonlinear in \mathbf{k} [4, 5]. Moreover, with increasing the well width, the band structure of HgTe QW could change from the normal to inverted regime, accompanied with a quantum phase transition [9, 10, 28]. In this paper, in order to take account of the unusual band structures and SOIs of HgTe QWs, we develop a theoretical method for calculating CPGE combining the eight-band $\mathbf{k} \cdot \mathbf{p}$ model with density matrix formalism. Using this method, we investigate the microscopic origin and pseudotensor of CPGE in HgTe QWs with non-parabolic, Dirac-like and inverted band structures. By introducing the SIA and BIA terms in the eight-band Hamiltonian, we discuss the interplay effect of them on the CPGE currents. The pure spin currents in HgTe QWs generated by normal incidence of linearly polarized light is also investigated using the similar formalism.

This paper is organized as follows: In Sec. II we describe the theoretical model based on the eight-band model and the density matrix formalism. In Sec. III, we discuss the microscopic origin and present the numerical results of SIA-induced CPGE in HgTe QWs. In Sec. IV, we introduce the influence of BIA, and consider the interplay effect of SIA and BIA on CPGE currents. In Sec. V, we turn to study the pure spin currents driven by linearly polarized light. Finally, A brief summary is given in Sec. VI.

II. BAND STRUCTURE MODEL AND THEORETICAL FORMALISM

As shown in Fig. 1(a), we consider a (001)-grown strain-free HgTe QW with x , y , z axis chosen to align the [100], [010] and [001] crystallographic orientations, respectively. Since the spin-splitting is an indispensable ingredient for the generation of CPGE [20], the Hamiltonian of HgTe QW, i.e., \hat{H}_0 , should contain a spacial inversion asymmetry part. So we can divided \hat{H}_0 as

$$\hat{H}_0 = \hat{H}_K + \hat{H}_A, \quad (1)$$

where \hat{H}_K and \hat{H}_A represent the inversion symmetry and asymmetry part of \hat{H}_0 , respectively. In this paper, \hat{H}_K is taken as the modified eight-band Kane Hamiltonian of a symmetric HgTe QW (see in Appendix A), which does not produce the spin-splitting. The source of spin-splitting comes from \hat{H}_A , which could either represent SIA or BIA. In HgTe-based QWs, SIA is found to be the dominant mechanism of spin-splitting [2]. So we will focus on the discussion of the SIA induced CPGE in Sec. III and the influence of BIA will be considered in Sec. IV.

The bulk HgTe is a semimetal with negative gap. If HgTe is sandwiched in between two barriers to form a QW, the band gap could be tuned from the negative

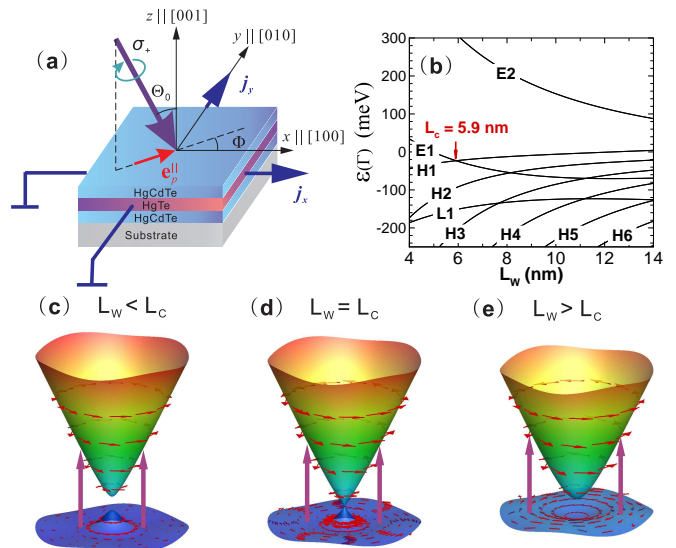


FIG. 1. (Color online) (a) Sketch of the right-handed circularly polarized (σ^+) light irradiating on HgTe QW. The CPGE currents is detected along the [100] and [010] crystallographic directions. The red arrow denotes the projection of light propagation direction unit vector on the QW plane, i.e., \mathbf{e}_p^{\parallel} . (b) Subband energies at Γ point of Brillouin zone as a function of well width L_w . The critical thickness for quantum transition is found to be $L_c = 5.9$ nm. (c)-(e) The 3D band structures and spin textures (red arrows) for HgTe QWs with different L_w : 5.0 nm, 5.9 nm and 9.0 nm, corresponding to normal, dirac-like, and inverted phase. The up purple arrows indicate the direct optical transitions.

regime to positive regime by quantum confinement effect. With increasing the thickness of HgTe layer, i.e., the well width L_w , a quantum phase transition takes place at the critical thickness $L_c = 5.9$ nm as shown in Fig. 1(b). If $L_w < L_c$, the E1 subband lies above H1 subband at Γ point like a normal semiconductor, corresponding to the normal phase of HgTe QW. Here, we should mention that the energy dispersions of normal HgTe QWs would show non-parabolic behavior due to the strong conduction-valence band coupling via narrow gap [see Fig. 1(c)]. If $L_w > L_c$, the order of E1 and H1 is inverted, i.e., H1 lies above E1, so the HgTe QW is in inverted phase. The band structure (bulk states) of inverted HgTe QW is displayed in Fig. 1(e). At the critical thickness, i.e., $L_w = L_c$, the low-energy dispersion of HgTe QW is a Dirac-like cone with zero gap [29] [see Fig. 1(d)]. All these band structures of HgTe QWs can be quantitatively described by \hat{H}_0 .

Consider the HgTe QW is illuminated by a beam of single-color polarized light with frequency ω . The incident angle and azimuth angle of light is denoted by Θ_0 and Φ , respectively [as sketched in Fig. 1(a)]. The total Hamiltonian can be written as

$$\hat{H} = \hat{H}_0 + \hat{V}(t), \quad (2)$$

where $\hat{V}(t)$ is the electron-radiation interaction.

$$\hat{V}(t) = \hat{S}e^{-i\omega t} + \hat{S}^\dagger e^{i\omega t}, \quad (3)$$

and

$$\hat{S} \equiv \frac{e}{im_0\omega} \mathbf{E} \cdot \hat{\mathbf{p}}, \quad (4)$$

Here $\hat{\mathbf{p}} = m_0\hat{\mathbf{v}}$ is the momentum operator. m_0 is the free electron mass, and $\hat{\mathbf{v}}$ is the velocity vector operator. In the representation of eight-band basis [Eq. (A1)], the three components of velocity operator, i.e., $\hat{v}_x, \hat{v}_y, \hat{v}_z$ are eight-by-eight matrix, and can be derived by [7]

$$\hat{v}_\alpha = \frac{1}{i\hbar} [\hat{r}_\alpha, \hat{H}_0], \quad (\alpha \in \{x, y, z\}). \quad (5)$$

\mathbf{E} is complex amplitude of light electric field. The three components of \mathbf{E} can be written as

$$\begin{aligned} E_x &= \frac{E_0}{\sqrt{2}} (t_p \cos \Theta \cos \Phi e^{i\varphi} - t_s \sin \Phi e^{-i\varphi}), \\ E_y &= \frac{E_0}{\sqrt{2}} (t_p \cos \Theta \sin \Phi e^{i\varphi} + t_s \cos \Phi e^{-i\varphi}), \\ E_z &= \frac{E_0}{\sqrt{2}} t_p \sin \Theta e^{i\varphi}. \end{aligned} \quad (6)$$

In Eq. (6), E_0 is the electric field amplitude in vacuum, Θ is the refraction angle determined by $\sin \Theta = \sin \Theta_0/n_r$, φ is half of the phase angle between the two perpendicular components of light electric field, t_p and t_s are the transmission coefficients for the p and s polarization components of the light electric field. E_0 is determined by the intensity of light via $E_0 = \sqrt{2I_0/(c_0 n_r \varepsilon_0)}$, where I_0 , c_0 , ε_0 and n_r are the intensity of light, light speed in vacuum, dielectric constant in vacuum, and the refraction index of QW, respectively. t_p and t_s can be found by Fresnel's formula: $t_p = 2 \cos \Theta / (n \cos \Theta + \sqrt{1 - \sin^2 \Theta / n^2})$, $t_s = 2 \cos \Theta / (\cos \Theta + \sqrt{n^2 - \sin^2 \Theta})$. Using Eq. (6), one can verify $i\mathbf{E} \times \mathbf{E}^* \propto t_p t_s P_{circ} |E_0|^2 \mathbf{e}_p$, where $P_{circ} \equiv (I_{\sigma^+} - I_{\sigma^-}) / (I_{\sigma^+} + I_{\sigma^-}) = \sin 2\varphi$ is the helicity of the incident light, and \mathbf{e}_p is the unit vector of the light propagation direction. Changing φ from 45° to 135° , the incident light could be continuously varied from right-handed circularly polarized (σ^+) to left-handed circularly polarized (σ^-). For the σ^+ (σ^-) light, its angular momentum has nonzero in-plane component parallel (antiparallel) to the projection of \mathbf{e}_p on the QW plane, i.e., denoted by \mathbf{e}_p^\parallel as in Fig. 1(a).

Density matrix formalism provides a quantum mechanics approach for the microscopic description of the linear and non-linear optical susceptibilities [30]. Following this formalism, other optical quantities, such as the expressions of circular photogalvanic currents and linear photogalvanic pure spin currents, can also be derived. We shall start from the Liouville equation which describes the time evolution of density matrix. Using the eigenstates of \hat{H}_0

as basis set, i.e., $\{|m, \mathbf{k}\rangle\}$, the Liouville equation can be written as

$$\frac{\partial \rho_{mn}}{\partial t} = -\frac{i}{\hbar} [\hat{H}, \hat{\rho}]_{mn} - \Gamma_{mn} [\rho_{mn} - \rho_{mn}^{eq}]. \quad (7)$$

In Eq. (7), $\hat{\rho}$ is the density operator, and we have used the notation $A_{mn} = A_{mn}(\mathbf{k}) \equiv \langle m, \mathbf{k} | \hat{A} | n, \mathbf{k} \rangle$ for the matrix elements of operator \hat{A} . ρ_{mn}^{eq} is the initial density matrix. At thermal equilibrium, $\rho_{mn}^{eq} = f_m \delta_{mn}$, where f_m is the Fermi distribution function. The second term on the right hand side of Eq. (7) is a phenomenological damping term. Γ_{nn} represents the decay rate for the nonequilibrium carriers in n -th subband, and $\Gamma_{mn}^{(m \neq n)}$ describes the dephasing rate of ρ_{mn} coherence. In this paper, we take $\Gamma_{nn} = 1/T_1$ with $T_1 = 200$ ps as a typical recombination life time of direct gap semiconductor. And $\Gamma_{mn}^{(m \neq n)} = 1/T_2$ with $T_2 = 1.3$ ps, which could cause a 1 meV level broadening in spectrums [31].

By treating $\hat{V}(t)$ as the perturbation, and expanding $\hat{\rho}$ as the sum of the zeroth, first, second order components: $\hat{\rho} \approx \hat{\rho}^{(0)} + \hat{\rho}^{(1)} + \hat{\rho}^{(2)}$, we have

$$\begin{aligned} \frac{\partial \rho_{mn}^{(0)}}{\partial t} &= -\frac{i}{\hbar} [\hat{H}_0, \hat{\rho}^{(0)}]_{mn} - \Gamma_{mn} (\rho_{mn}^{(0)} - \rho_{mn}^{eq}), \\ \frac{\partial \rho_{mn}^{(1)}}{\partial t} &= -\frac{i}{\hbar} [\hat{H}_0, \hat{\rho}^{(1)}]_{mn} - \frac{i}{\hbar} [\hat{V}(t), \hat{\rho}^{(0)}]_{mn} - \Gamma_{mn} \rho_{mn}^{(1)}, \\ \frac{\partial \rho_{mn}^{(2)}}{\partial t} &= -\frac{i}{\hbar} [\hat{H}_0, \hat{\rho}^{(2)}]_{mn} - \frac{i}{\hbar} [\hat{V}(t), \hat{\rho}^{(1)}]_{mn} - \Gamma_{mn} \rho_{mn}^{(2)}. \end{aligned} \quad (8)$$

We are interested in the second order steady-state solution of Eq. (8), i.e., $\rho_{mn}^{(2)}(t)$ with $t \rightarrow \infty$, which is found to be

$$\begin{aligned} \rho_{mn}^{(2)\infty}(\mathbf{k}) &\equiv \rho_{mn}^{(2)}(t \rightarrow \infty) = -\frac{1}{\hbar^2(\omega_{mn} - i\Gamma_{mn})} \\ &\times \sum_q S_{mq} (S^\dagger)_{qn} \left(\frac{f_q - f_n}{\omega_{qn} + \omega - i\Gamma_{qn}} + \frac{f_q - f_m}{\omega_{mq} - \omega - i\Gamma_{mq}} \right) \\ &+ \sum_q (S^\dagger)_{mq} S_{qn} \left(\frac{f_q - f_m}{\omega_{mq} + \omega - i\Gamma_{mq}} + \frac{f_q - f_n}{\omega_{qn} - \omega - i\Gamma_{qn}} \right). \end{aligned} \quad (9)$$

Here $\omega_{mn} \equiv \varepsilon_m(\mathbf{k}) - \varepsilon_n(\mathbf{k})$, and $\varepsilon_m(\mathbf{k})$ is the eigenenergy of \hat{H}_0 . S_{mn} and $(S^\dagger)_{mn}$ are the matrix elements of \hat{S} and \hat{S}^\dagger . In principle, m, n, q should run over all subbands of HgTe QW. However, for the absorption of single-color light, only a few subbands (less than 10 subbands) with energy differences in the range of photon energy needs to be taken into account, because optical process obeys energy conservation law. After obtaining the set of eigenenergies and eigenstates of HgTe QWs, i.e., $\{\varepsilon_m(\mathbf{k})\}$, $\{|m, \mathbf{k}\rangle\}$ by Eq. (A4), $\rho_{mn}^{(2)\infty}(\mathbf{k})$ can be calculated according to Eq. (9).

The density matrix can be used to evaluate the expectation value of an arbitrary operator \hat{O}

$$\langle \hat{O} \rangle = \sum_{\mathbf{k}} \text{tr}\{\hat{O}\hat{\rho}\} = \sum_{\mathbf{k}, m, n} \rho_{mn}(\mathbf{k}) \langle n, \mathbf{k} | \hat{O} | m, \mathbf{k} \rangle. \quad (10)$$

Note Eq. (10) contains a Brillouin-zone integration over the in-plane \mathbf{k} space. In order to achieve numerical results with acquired accuracy, over 150000 states on in-plane \mathbf{k} grids needs to be calculated. For each \mathbf{k} , a $(16N+8)$ -by- $(16N+8)$ Hamiltonian matrix generated by plane wave expansion method [see Eq.(A5)] is required to be diagonalized. A parallel numerical program based on Message Passing Interface (MPI) is designed to accelerate this calculation.

III. CIRCULAR PHOTOGAVALNIC CHARGE CURRENTS

In this section, we discuss the microscopic origin and numerical results of SIA-induced CPGE currents. In low-dimensional semiconductors, SIA may arise from the asymmetrical heterostructure materials, confining potentials or dopings, as well as the external or built-in electric fields. For the single conduction band model, SIA is usually described by a \mathbf{k} -linear term, or so-called Rashba term. In eight-band $\mathbf{k} \cdot \mathbf{p}$ Hamiltonian, SIA can be introduced by a static electric field \mathcal{F} along z axis

$$\hat{H}_A = \hat{H}_{SIA} = -e\mathcal{F}z. \quad (11)$$

The effect of \hat{H}_{SIA} is producing the Rashba-type spin-splitting of band structures. Different from the conventional Rashba term, the spin-splitting induced by \hat{H}_{SIA} is nonlinear in \mathbf{k} , because the kinetic energy of electrons in HgTe QWs is comparable to the narrow band gap [4, 5]. This feature is not present in the single band model, but here is taken into account within the eight-band model.

Applying Eq. (10), the photogalvanic charge currents can be calculated by

$$\mathbf{j} = -e \sum_{\mathbf{k}, m, n} \rho_{mn}(\mathbf{k}) \mathbf{v}_{nm}(\mathbf{k}). \quad (12)$$

Because the Hamiltonian of HgTe QW is a time-reversal invariant, it guarantees the Kramers degeneracy, i.e., $\varepsilon_n(\mathbf{k}) = \varepsilon_{\bar{n}}(-\mathbf{k})$. Here and in the following, a bar above the subband index denotes the subband with the opposite spin. By applying the time reversal operation, we can demonstrate $\mathbf{v}_{mn}(\mathbf{k}) = -\mathbf{v}_{\bar{m}\bar{n}}^*(-\mathbf{k}) = -\mathbf{v}_{\bar{n}\bar{m}}(-\mathbf{k})$. Using these properties, Eq. (12) can be split as

$$\begin{aligned} \mathbf{j} &= -\frac{e}{2} \sum_{\mathbf{k}, m, n} [\rho_{mn}(\mathbf{k}) \mathbf{v}_{nm}(\mathbf{k}) + \rho_{mn}(-\mathbf{k}) \mathbf{v}_{nm}(-\mathbf{k})] \\ &= -\frac{e}{2} \sum_{\mathbf{k}, m, n} [\rho_{mn}(\mathbf{k}) \mathbf{v}_{nm}(\mathbf{k}) - \rho_{mn}(-\mathbf{k}) \mathbf{v}_{\bar{n}\bar{m}}(\mathbf{k})]. \end{aligned} \quad (13)$$

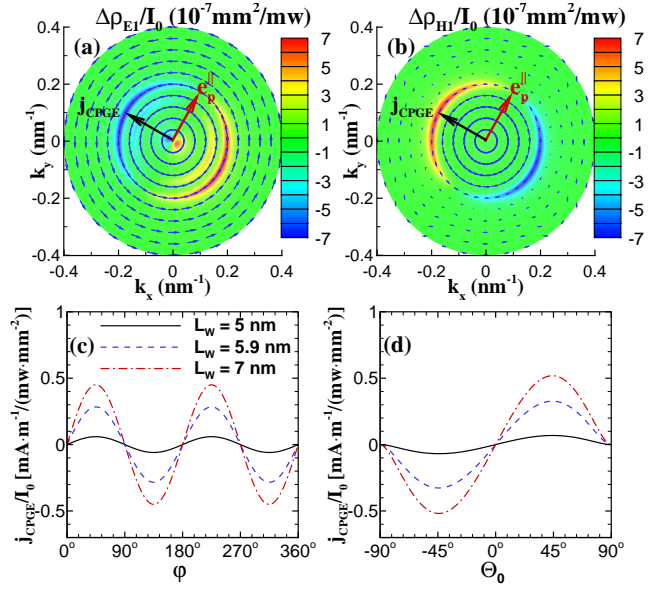


FIG. 2. (a) and (b) (Color online) Calculated $\mathfrak{B}_n(\mathbf{k})$ of RSOI (minor blue arrows) and $\Delta\rho_{nn}(\mathbf{k})$ (contour plot) of a 5.9 nm HgTe QW with $\mathcal{F} = 80$ kV/cm, for $n = E1$ and $H1$ subband respectively. They are induced by a σ^+ light with $\hbar\omega = 129$ meV, $\Theta_0 = 30^\circ$ and $\Phi = 60^\circ$. The red arrows indicate the projection of light prorogation direction in the QW plane and the black arrows indicate the direction of CPGE current. (c) and (d) The magnitudes of photocurrent as a function of half phase angle φ ($\Theta_0 = 30^\circ$) and the incident angle of light Θ_0 ($\varphi = 45^\circ$), for HgTe QWs with different QW widths.

Then, we change the dummy subscripts m, n of the second term by \bar{n}, \bar{m} , and get

$$\mathbf{j} = -\frac{e}{2} \sum_{\mathbf{k}, m, n} [\rho_{mn}(\mathbf{k}) - \rho_{\bar{n}\bar{m}}(-\mathbf{k})] \mathbf{v}_{nm}(\mathbf{k}). \quad (14)$$

Eq. (14) demonstrates that the photocurrents come from the non-symmetrical distribution of photo-excited density matrix at \mathbf{k} and $-\mathbf{k}$ points. We can describe the asymmetrical part of density matrix by $\Delta\rho_{mn}(\mathbf{k}) \equiv \rho_{mn}(\mathbf{k}) - \rho_{\bar{n}\bar{m}}(-\mathbf{k})$. In steady condition, only the second order density matrix contributes to the asymmetry, which gives $\Delta\rho_{mn}(\mathbf{k}) = \rho_{mn}^{(2)\infty}(\mathbf{k}) - \rho_{\bar{n}\bar{m}}^{(2)\infty}(-\mathbf{k})$. Due to the spin-dependent selection rule, the circularly polarized light would give rise to different transition rates for $|m(n), \mathbf{k}\rangle \leftrightarrow |q, \mathbf{k}\rangle$ from $|\bar{m}(\bar{n}), -\mathbf{k}\rangle \leftrightarrow |\bar{q}, -\mathbf{k}\rangle$, thus break the symmetrical distribution of $\rho_{mn}(\mathbf{k})$ [or cause $\Delta\rho_{mn}(\mathbf{k}) \neq 0$] according to Eq. (9). As a consequence, a net charge current would emerge following Eq. (14). This process is equivalent to the transformation of photon angular-momenta into translational motion of free carriers [16].

In order to manifest the role of SOI in the generation of CPGE, we introduce the notion of effective magnetic field $\mathfrak{B}_n(\mathbf{k})$ of SOI [32] (see the details in Appendix C). $\mathfrak{B}_n(\mathbf{k})$ can be regarded as the effective magnetic field felt by electron with state $|n, \mathbf{k}\rangle$ as a result of spin-orbit

coupling. The magnitude and direction of $\mathfrak{B}_n(\mathbf{k})$ can describe the SOI spin-splitting of n -th subband and the spin orientation of the upper spin branch, respectively. In Fig. 2(a) and 2(b), we plot the calculated effective magnetic fields $\mathfrak{B}_n(\mathbf{k})$ and the asymmetrical parts of diagonal density matrix elements $\Delta\rho_{nn}(\mathbf{k})$, for $n = \text{E1}$ and H1 , respectively. The picture of $\Delta\rho_{nn}(\mathbf{k})$ can be viewed as the unbalanced carrier density distribution in \mathbf{k} -space for n -th subband. The σ^+ light at oblique incidence has a non-zero in-plane angular momentum component along \mathbf{e}_p^\parallel , so it will excite more E1 (H1) states with $\mathfrak{B}_n(\mathbf{k})$ parallel (antiparallel) to \mathbf{e}_p^\parallel . For HgTe QWs with SIA only, the systems hold C_{4v} point group symmetry, restricting $\mathfrak{B}_n(\mathbf{k})$ perpendicular to \mathbf{k} for most E1 and H1 states. Therefore we can see the maximum of $\Delta\rho_{nn}(\mathbf{k})$ will appear at the direction perpendicular to \mathbf{e}_p^\parallel in \mathbf{k} space. Note that though E1 and H1 states have opposite signs of $\Delta\rho_{nn}(\mathbf{k})$, their effective masses and velocities are also opposite in signs, so they can contribute to the net charge currents along the same direction perpendicular to \mathbf{e}_p^\parallel , instead of cancelling with each other. In Fig. 2(c), we can see the calculated photocurrents clearly exhibit the characteristic feature of CPGE, i.e, the sign dependency of light's helicity. Fig. 2(d) shows the photocurrents as a function of incident angle Θ_0 . We find the most effective incident angle to generate CPGE currents is $\Theta_0 = \pm 45^\circ$. Because at this incident angle, the refraction light have the largest in-plane angular momentum component, as determined by the Fresnel's formula. In addition, we find the photocurrents increase with the width of well. This is because the wider QW have larger spin-splitting under the same SIA electric field.

Phenomenologically, the photogalvanic currents can be described by [15]

$$j_\lambda = \sum_{\alpha, \beta} \chi_{\lambda\alpha\beta} E_\alpha E_\beta^*, \quad (15)$$

where $\chi_{\lambda\alpha\beta}$ is a third-rank phenomenological tensor. For the in-plane photocurrents, $\lambda \in \{x, y\}$ and $\alpha, \beta \in \{x, y, z\}$. Inserting Eq. (9) into Eq. (12) and comparing with Eq. (15), we can find the microscopic expression for $\chi_{\lambda\alpha\beta}$ is

$$\begin{aligned} \chi_{\lambda\alpha\beta} = & \frac{e^3}{\omega^2 \hbar^2} \sum_{\mathbf{k}} \sum_{mnq} (f_q - f_m) \\ & \times [v_{mq}^\alpha v_{qn}^\beta v_{nm}^\lambda \mathcal{L}_{mnq}(\omega) + v_{nq}^\alpha v_{qm}^\beta v_{mn}^\lambda \mathcal{L}_{mnq}^*(\omega) \\ & + v_{qn}^\alpha v_{mq}^\beta v_{nm}^\lambda \mathcal{L}_{mnq}(-\omega) + v_{qm}^\alpha v_{nq}^\beta v_{mn}^\lambda \mathcal{L}_{mnq}^*(-\omega)], \end{aligned} \quad (16)$$

where $\mathcal{L}_{mnq}(\omega) \equiv 1/[(\omega_{mn} - i\Gamma_{mn})(\omega_{mq} - \omega - i\Gamma_{mq})]$. From Eq. (16), we can verify $\chi_{\lambda\alpha\beta} = \chi_{\lambda\beta\alpha}^*$. This property allows one to decompose Eq. (15) into two terms which link to the symmetric and anti-symmetric sum of

$E_\alpha E_\beta^*$, respectively:

$$\begin{aligned} j_\lambda = & \sum_{\alpha\beta} \text{Re}(\chi_{\lambda\alpha\beta}) \frac{E_\alpha E_\beta^* + E_\alpha E_\beta^*}{2} \\ & + i \sum_{\alpha\beta} \text{Im}(\chi_{\lambda\alpha\beta}) \frac{E_\alpha E_\beta^* - E_\alpha E_\beta^*}{2}. \end{aligned} \quad (17)$$

The first and second term on the right-hand side of Eq. (17) describe the linear photogalvanic effect and circular photogalvanic effect, or LPGE and CPGE, respectively. In (001)-oriented HgTe QWs, experiments show the LPGE currents are very small compared to the CPGE currents [23]. In our calculation, we also find the LPGE currents are negligible. Therefore we can simply drop the LPGE term, and rewrite Eq. (17) as a commonly referred form [17, 23]

$$j_\lambda = \sum_{\mu} \gamma_{\lambda\mu} i(\mathbf{E} \times \mathbf{E}^*)_{\mu}, \quad (18)$$

where $\gamma_{\lambda\mu}$ ($\lambda, \mu \in \{x, y\}$) is a second-rank pseudotensor. Using the Levi-Civita antisymmetric tensor $\varepsilon_{\alpha\beta\lambda}$, we can write $\gamma_{\lambda\mu} = \text{Im}(\chi_{\lambda\alpha\beta}) \varepsilon_{\alpha\beta\mu}$. For the HgTe QW with SIA only, the C_{4v} symmetry requires $\gamma_{yx} = -\gamma_{xy}$ be the only nonzero components of $\gamma_{\lambda\mu}$.

In Fig. 3, we present the calculated band structures for HgTe QWs with different quantum phases, the corresponding spectrums of γ_{yx} , and each contributions from different subband-subband transitions. We can see the spectrums of γ_{yx} are sensitively dependent on the band structures and spin-splitting. In wider HgTe QW, the Rashba spin-splitting are larger and more subbands could be involved in the optical transition. Therefore the maximum of γ_{yx} increases with L_w . For all QWs, the largest contribution to γ_{yx} comes from the transition of the top valence subband to the bottom conduction subband. Because in these subbands, the photo-excited carriers have the largest \mathbf{k} and spin-splitting compared to other subbands. Interestingly, we find the CPGE current in 9 nm HgTe QW is significantly enhanced at a certain range of spectrum (40-100 meV). This is because in the inverted phase regime, the band structure of HgTe QW could be heavily inverted so that the H1 and H2 become the bottom conduction and top valence subband, respectively. While H2 has a distorted energy dispersion that it even bends upwards for a range of $|\mathbf{k}|$ [0-0.4 nm⁻¹ for 9 nm HgTe QW in Fig. 3(f)]. This distorted dispersion gives rise to a great increase of Joint density of states at the corresponding energy spectrum. As a result, the optical absorption and CPGE current is evidently enhanced (about 2-4 times larger). This feature could be taken advantages in the designment of high efficiency ellipticity detector in infrared and terahertz region [14].

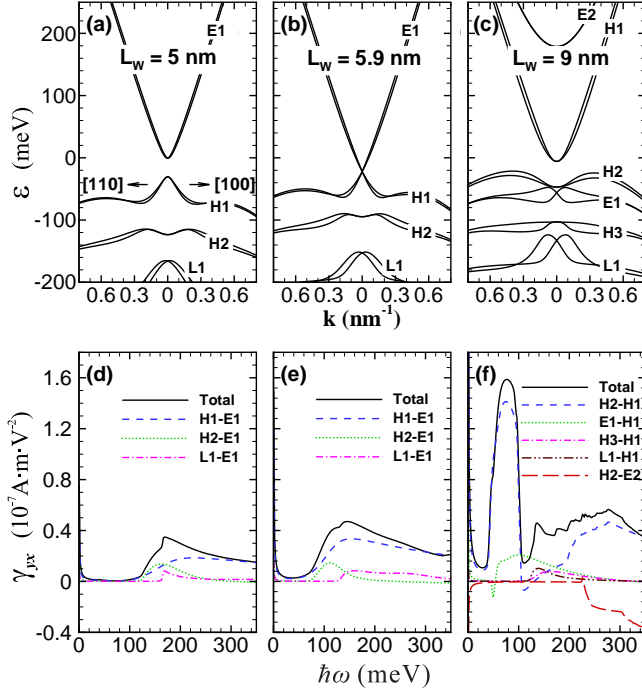


FIG. 3. (Color online) (a)-(c) The band structures of HgTe QWs with SIA ($\mathcal{F} = 80$ kV/cm), for $L_w = 5.0$ nm, 5.9 nm, 9.0 nm respectively. (d)-(f) The calculated spectrums of γ_{xy} with respect to (a)-(c). The black solid lines are the total spectrums of γ_{xy} including all contributions, and the other lines are each contributions from different subband-subband transitions.

IV. INFLUENCE OF BULK INVERSION ASYMMETRY

Hg_{1-x}Cd_xTe has a zinc-blende structure, which lacks a center of inversion. Therefore the SOI could produce a BIA spin-splitting even in the absence of SIA. In HgTe QW, the BIA effect is less explored, because it is considered to be smaller than that of SIA. However, introducing BIA terms in the Hamiltonian would lead to a qualitatively different symmetry of system. This could be reflected on the CPGE currents.

In this section, we discuss the BIA effect on CPGE by adding the BIA term \hat{H}_{BIA} into eight-band Hamiltonian, i.e., setting $\hat{H}_A = \hat{H}_{SIA} + \hat{H}_{BIA}$. The BIA term is known as the Dresselhaus k^3 term for the single conduction band model. For the eight-band model, there are two kinds of BIA terms, which are the Kane's off-diagonal terms with parameters B_{8v}^\pm, B_{7v} [32, 33], and the Γ_8 band \mathbf{k} -linear terms with parameter C_k [34, 35]. These BIA terms can be derived by the theory of invariants [32, 36]. The form of \hat{H}_{BIA} and BIA parameters are presented in Appendix B.

For HgTe QWs with BIA only, i.e., let $\hat{H}_A = \hat{H}_{BIA}$, the symmetry of system belongs to D_{2d} point group, which can be reflected by the effective magnetic field of E1 subband, i.e., $\mathfrak{B}_{E1}(\mathbf{k})$ in Fig. 4(a). Because $\mathfrak{B}_{E1}(\mathbf{k})$ of BIA

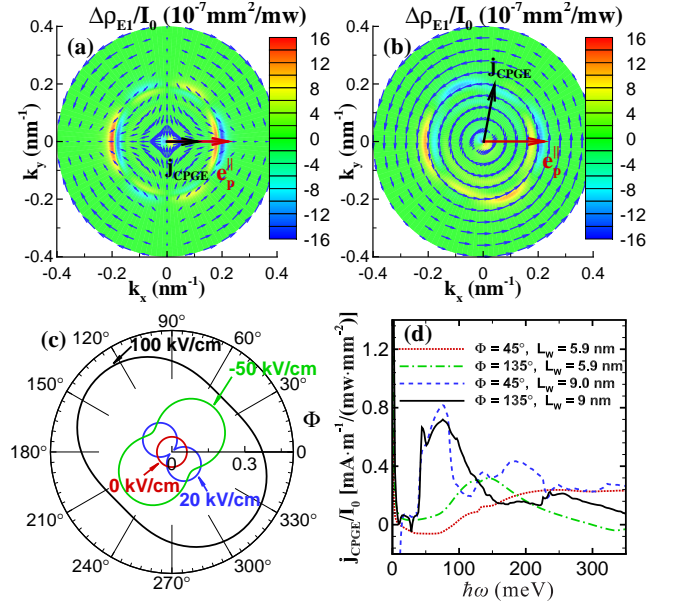


FIG. 4. (Color online) (a) Calculated $\mathfrak{B}_{E1}(\mathbf{k})$ (minor blue arrows) and $\Delta\rho_{E1}(\mathbf{k})$ (contour color) for 5.9 nm HgTe QW with BIA only. The incident light is right-hand circularly polarized, with $\hbar\omega = 129$ meV, $\Phi = 0^\circ$, and $\Theta_0 = 30^\circ$. (b) The same as (a) but the QW has both BIA and SIA ($\mathcal{F} = 80$ kV/cm). (c) The magnitude of CPGE current [in unit of $\text{mA}\cdot\text{m}^{-1} \times I_0/(\text{mW}\cdot\text{mm}^{-2})$] as a function of the incident azimuth angle Φ , for 5.9 nm QW with BIA and different SIA electric field $\mathcal{F} = 0, 20, 100, -50$ kV/cm. The photon energy is $\hbar\omega = 160$ meV. (d) The CPGE current spectrums for $\Phi = 45^\circ$ ($\mathbf{e}_p^\parallel \parallel [110]$) and 135° ($\mathbf{e}_p^\parallel \parallel [\bar{1}10]$), in 5.9 nm and 9 nm HgTe QW ($\mathcal{F} = 60$ kV/cm), respectively.

is parallel (antiparallel) to \mathbf{k} at $[100]$ ($[\bar{1}00]$) direction, if the incident azimuth angle $\Phi = 0^\circ$, i.e., $\mathbf{e}_p^\parallel \parallel [100]$, the σ^+ light would excite asymmetrical distribution of $\Delta\rho_{mn}(\mathbf{k})$ along $[100]$ - $[\bar{1}00]$ direction [see the example of the diagonal element of $\Delta\rho_{mn}(\mathbf{k})$ for E1 subband, i.e., $\Delta\rho_{E1}(\mathbf{k})$ in Fig. 4(a)]. As a result, a net charge current along $[100]$ direction will be produced, which corresponds to a nonzero pseudotensor component γ_{xx} . Symmetry analysis shows $\gamma_{xx} = -\gamma_{yy}$ are the only nonzero components of $\gamma_{\lambda\mu}$ for QWs with BIA only.

For HgTe QWs with both BIA and SIA exist, the symmetry of system is reduced to C_{2v} point group, which is displayed by $\mathfrak{B}_{E1}(\mathbf{k})$ in Fig. 4(b). The σ^+ light with $\mathbf{e}_p^\parallel \parallel [100]$ could excite CPGE currents which have both $[100]$ and $[010]$ components, because $\mathfrak{B}_{E1}(\mathbf{k})$ can be viewed as the superposition of RSOI and DSOI magnetic effective fields. In this case, there are two types of independent components of $\gamma_{\lambda\mu}$, which are $\gamma_{xx} = -\gamma_{yy}$ and $\gamma_{yx} = -\gamma_{xy}$, respectively.

Due to the interference of RSOI and DSOI, the CPGE currents exhibit anisotropic behaviors about the azimuth angle Φ of oblique incident light, which are exhibited in Fig. 4(c). We can see the minimum and maximum of CPGE currents appear at $\Phi = 45^\circ$ or 135° , and the de-

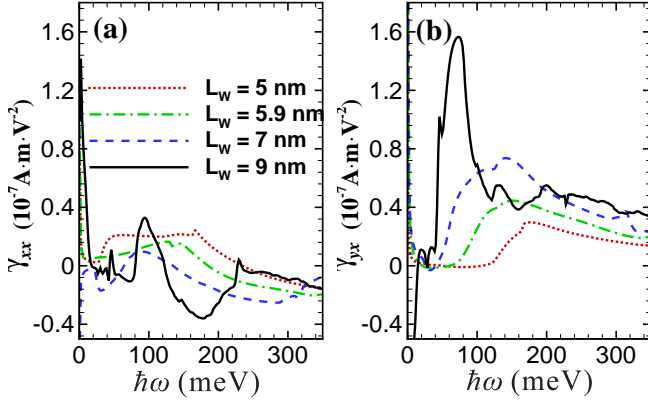


FIG. 5. (Color online) (a) and (b) The spectrums of γ_{xx} and γ_{yx} , respectively, for 5 nm, 5.9 nm, 7 nm, 9 nm HgTe QWs with both BIA and SIA ($\mathcal{F} = 80$ kV/cm).

gree of anisotropy can be tuned by changing the SIA electric field \mathcal{F} . One can achieve the strongest anisotropy of CPGE currents at certain conditions when $|\gamma_{xx}| \approx |\gamma_{yx}|$ [e.g., see the blue line for $\mathcal{F} = 20$ kV/cm in Fig. 4(c)]. Under these conditions, the RSOI happens to cancel DSOI at $\mathbf{k} \parallel [110]$ (or $[\bar{1}10]$), so that there could be many interesting phenomena emerge such as the suppression of weak antilocalization [37], the disappearance of SdH oscillation beating [38], the very long spin relaxation time for spins oriented $[110]$ or $[\bar{1}10]$ [39], and the persistent spin helix [40, 41]. Here, we suggest the anisotropy of CPGE about the azimuth angle of incident light could offer another mean to find these conditions when RSOI could cancel DSOI.

In Fig. 4(d), we give the calculated CPGE current spectrums for incident light with $\mathbf{e}_p \parallel [110]$ and $[\bar{1}10]$ in 5.9 nm and 9 nm HgTe QWs, respectively. In general, the spectrums of CPGE currents are not equal for $\mathbf{e}_p \parallel [110]$ and $\mathbf{e}_p \parallel [\bar{1}10]$ because of the anisotropy, but there are crossing points in spectrums where CPGE currents are equal [which means CPGE is isotropic about Φ]. So we can see the anisotropy of CPGE is also dependent on the photon energy of incident light. Comparing the CPGE spectrums of 5 nm and 9 nm HgTe QW, we find the spectrums difference between $\mathbf{e}_p \parallel [110]$ and $\mathbf{e}_p \parallel [\bar{1}10]$ is larger in 5 nm QW. This is because the influence of BIA is more prominent in narrower QWs, implying the anisotropy behavior of CPGE can be more easily observed in narrow QWs.

Substituting the components of \mathbf{E} in Eq. (18) by Eq. (6), we can obtain a simple phenomenological expression for the photocurrents

$$\begin{aligned} j_x &= E_0^2 t_s t_p \sin \Theta P_{circ} (\gamma_{xx} \cos \Phi - \gamma_{yx} \sin \Phi), \\ j_y &= -E_0^2 t_s t_p \sin \Theta P_{circ} (\gamma_{xx} \sin \Phi - \gamma_{yx} \cos \Phi). \end{aligned} \quad (19)$$

If one choose the configuration $x \parallel [100]$ and $y \parallel [100]$ [as in Fig. 1(a)], by using Eq. (19) we can demonstrate the

ratio of CPGE currents satisfy

$$\frac{j_y(\mathbf{e}_p \parallel x)}{j_x(\mathbf{e}_p \parallel x)} = \frac{j_x(\mathbf{e}_p \parallel y)}{j_y(\mathbf{e}_p \parallel y)} = \frac{\gamma_{yx}}{\gamma_{xx}}. \quad (20)$$

If one choose another configuration, i.e., $x' \parallel [110]$ and $y' \parallel [\bar{1}10]$, we can find $j_{x'}(\mathbf{e}_p \parallel x') = j_{y'}(\mathbf{e}_p \parallel y') = 0$, and

$$\frac{j_{y'}(\mathbf{e}_p \parallel x')}{j_{x'}(\mathbf{e}_p \parallel y')} = \frac{\gamma_{xx} - \gamma_{yx}}{\gamma_{xx} + \gamma_{yx}}. \quad (21)$$

Giglberger et al. have shown that γ_{yx}/γ_{xx} obtained by CPGE is very close to the RD Ratio measured by spin-galvanic effect [22]. Since then CPGE has been widely applied in the separation of the RSOI and DSOI [21, 22, 42, 43]. However, we should mention that γ_{yx}/γ_{xx} may not always equal to the RD ratio, because $\gamma_{\lambda\mu}$ have very complex dependence on the photon energy, just as the spectrum of γ_{xx} and γ_{yx} displayed in Fig. 5. Our calculation show CPGE currents are not only dependent on the spin-splitting of conduction and valence bands, but also on the Joint Density of States and the number of subbands involved in the optical transition, which makes the spectrums of $\gamma_{\lambda\mu}$ very complicated. As a specific example, we can see there are independent peaks occurrences in the γ_{xx} and γ_{yx} spectrums of 9 nm HgTe QW, which lead to the value of γ_{yx}/γ_{xx} could vary in a wide range. Therefore γ_{yx}/γ_{xx} may lose its validity for reflecting the real RD ratio, especially in materials have band structure abnormalities as the 9 nm HgTe QW. To quantitatively analyse the CPGE experimental results of materials with unusual band structures, theory based on multi-band model is necessary.

V. PURE SPIN CURRENTS INDUCED BY LINEARLY POLARIZED LIGHT

A pure spin current (PSC) is usually defined by a spin flow without net charge current. In non-centrosymmetric semiconductors, PSCs can be generated by illuminating a single-color linearly polarized light on the sample [44, 45]. Because linearly polarized light can be regarded as the coherent superposition of two circularly polarized lights with opposite helicities and equal strengths, it can drive equal numbers of spin-up and spin-down carriers travels in the opposite directions as by CPGE. In this situation, the net charge currents are cancelled but the spins are transported, i.e., the PSCs are formed. The linearly polarized light induced PSCs have been demonstrated by using the spatially resolved pump-probe technique [2]. This method provides an optical mean to inject PSCs into semiconductors.

In this section, by setting $\varphi = 0$ and $\Theta_0 = 0$ in Eq. (6) to get a linearly polarized light at normal incidence, we can investigate the linear photogalvanic PSCs in HgTe QWs via density matrix formalism. In Eq. (6), the linear

polarization direction of light can be changed by Φ , and $\Phi = 0^\circ$ gives a light linearly polarized along [110] direction. By utilizing the the photo-excited density matrix, the PSCs can be calculated by

$$j_\alpha^\beta = \sum_{\mathbf{k}, m, n} \rho_{mn}(\mathbf{k}) \langle n, \mathbf{k} | \hat{j}_\alpha^\beta | m, \mathbf{k} \rangle. \quad (22)$$

Here j_α^β stands for the spin current moving along α direction and spins orienting β direction, and $\hat{j}_\alpha^\beta \equiv \frac{\hbar}{4}(\hat{v}_\alpha \hat{\Sigma}_\beta + \hat{\Sigma}_\beta \hat{v}_\alpha)$ is the corresponding spin current operator. \hat{v}_α is the α component of velocity operator defined in Eq. (5), and $\hat{\Sigma}_\beta$ is the β component of eight-band spin matrices [46]. The phenomenological expression of photogalvanic spin currents write as

$$j_\alpha^\beta = \sum_{\gamma\delta} \mu_{\alpha\beta\gamma\delta} E_\gamma E_\delta^*. \quad (23)$$

Here we consider the in-plane spin currents induced by normal incidence of light, therefore $\alpha, \beta, \gamma, \delta \in \{x, y\}$. $\mu_{\alpha\beta\gamma\delta}$ is a fourth-rank tensor. For the linearly polarized light, $E_\gamma E_\delta^* \equiv E_\gamma E_\delta$ is real, which restricts $\mu_{\alpha\beta\gamma\delta}$ is also real and symmetric with respect to the interchange of the last two indices, i.e., $\mu_{\alpha\beta\gamma\delta} = \mu_{\alpha\beta\delta\gamma}$. Using Eq. (9), we can derive the microscopic expression for $\mu_{\alpha\beta\gamma\delta}$ is

$$\begin{aligned} \mu_{\alpha\beta\gamma\delta} &= \frac{e^2}{\omega^2 \hbar^2} \sum_{\mathbf{k}} \sum_{m, n, q} (f_m - f_q) \\ &\times [j_{\alpha, nm}^\beta v_{mq}^\gamma v_{qn}^\delta \mathcal{L}_{m, n, q}(\omega) + j_{\alpha, mn}^\beta v_{nq}^\gamma v_{qm}^\delta \mathcal{L}_{m, n, q}^*(\omega) \\ &+ j_{\alpha, nm}^\beta v_{qn}^\gamma v_{mq}^\delta \mathcal{L}_{m, n, q}(-\omega) + j_{\alpha, mn}^\beta v_{qm}^\gamma v_{nq}^\delta \mathcal{L}_{m, n, q}^*(-\omega)], \end{aligned} \quad (24)$$

where $j_{\alpha, mn}^\beta \equiv \langle m, \mathbf{k} | \hat{j}_\alpha^\beta | n, \mathbf{k} \rangle$ and the definition of $\mathcal{L}_{m, n, q}(\omega)$ is the same as in Eq. (16).

Symmetry analysis shows that there could be six independent components of $\mu_{\alpha\beta\gamma\delta}$ for a general HgTe QWs. They are

$$\begin{aligned} \mu_1 &= \mu_{xxxx} = -\mu_{yyyy}, \\ \mu_2 &= \mu_{yyxx} = -\mu_{xxyy}, \\ \mu_3 &= \mu_{xyxx} = -\mu_{yxyy}, \\ \mu_4 &= \mu_{yxxx} = -\mu_{xyyy}, \\ \mu_5 &= \mu_{xxyy} = -\mu_{yyxy} = \mu_{xyyx} = -\mu_{yxyx}, \\ \mu_6 &= \mu_{xyxy} = \mu_{yyxx} = -\mu_{yxxy} = -\mu_{xyyx}. \end{aligned}$$

If there is only SIA in the system, we find $\mu_1, \mu_2, \mu_6 = 0$ but $\mu_3, \mu_4, \mu_5 \neq 0$, which means the [100]-linearly-polarized light could excite two nonzero PSCs, i.e., j_x^y and j_y^x respectively. Otherwise, if only BIA exists, we find $\mu_1, \mu_2, \mu_6 \neq 0$, but $\mu_3, \mu_4, \mu_5 = 0$. j_x^x and j_y^y would be the nonzero PSCs under the irradiation of [100]-linearly-polarized light. If both SIA and BIA are present, all the components μ_1, \dots, μ_6 are nonzero. So [100]-linearly-polarized would give rise to four nonzero PSCs, which are j_x^x, j_x^y, j_y^x and j_y^y , respectively.

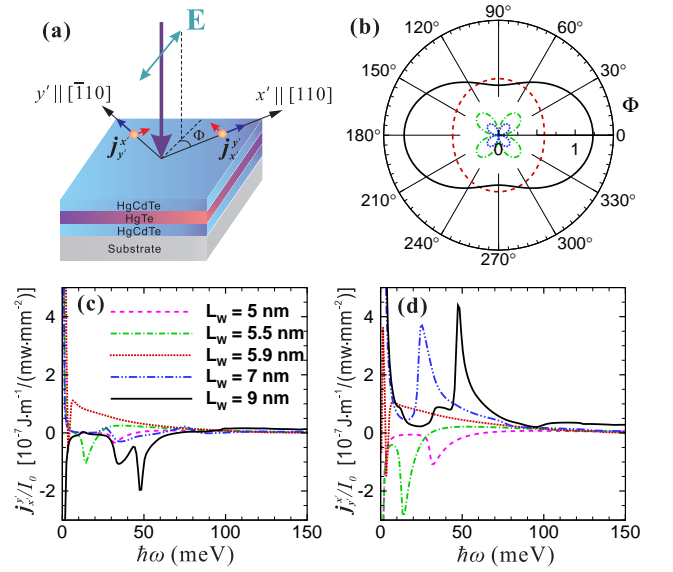


FIG. 6. (Color online) (a) Sketch of configuration for the generation of PSCs in HgTe QW by normally irradiating the linearly polarized light. (b) The four PSCs [in unit of $10^{-7} \text{ J}\cdot\text{m}^{-1} \times I_0 / (\text{mw}\cdot\text{mm}^{-2})$]: $j_{x'}^{y'}$ (red dashed line), $j_{y'}^{x'}$ (black solid line), $j_{x'}^{x'}$ (green dashdot line) and $j_{y'}^{y'}$ (blue dotted line) as a function of the linear polarization direction of light, in 9 nm HgTe QW. The incident photon energy is $\hbar\omega = 45 \text{ meV}$. (c) and (d) The spectrums of $j_{x'}^{y'}$ and $j_{y'}^{x'}$ induced by [110]-linearly-polarized light, respectively, for HgTe QWs with different well widths. In all above panels, we have assumed the HgTe QWs have both BIA and SIA ($\mathcal{F} = 80 \text{ kV/cm}$).

Alternatively, we can choose another configuration with $x' \parallel [110]$ and $y' \parallel [\bar{1}10]$ for the description of PSCs [as sketched in Fig. 6(a)]. The relationship between $j_{\alpha'}^{\beta'}$ ($\alpha', \beta' \in \{x', y'\}$) and j_α^β ($\alpha, \beta \in \{x, y\}$) can be found by coordinates rotation. Let $\mathbb{R}(\vartheta)$ be the in-plane rotation matrix of a rotation angle ϑ

$$\mathbb{R}(\vartheta) = \begin{pmatrix} \cos \vartheta & \sin \vartheta \\ -\sin \vartheta & \cos \vartheta \end{pmatrix}, \quad (25)$$

then the relation is found to be

$$j_{\alpha'}^{\beta'} = \sum_{\alpha\beta} \mathbb{R}_{\alpha'\alpha}(\frac{\pi}{4}) \mathbb{R}_{\beta'\beta}(\frac{\pi}{4}) j_\alpha^\beta. \quad (26)$$

In Fig. 6(b) we plot the four in-plane PSCs, i.e., $j_{x'}^{y'}$, $j_{y'}^{x'}$, $j_{x'}^{x'}$ and $j_{y'}^{y'}$, in 9 nm HgTe QW as a function of the light's linear polarization direction Φ . We can see $j_{x'}^{x'}$ and $j_{y'}^{y'}$ are zero when the incident light is linearly polarized along [110] ($\Phi = 0^\circ, 180^\circ$) or $[\bar{1}10]$ ($\Phi = 90^\circ, 270^\circ$), but they have finite values along other directions. For QWs with both BIA and SIA exist, the four PSCs are not equivalent to each other, since the symmetry of QW is as low as C_{2v} point group.

If we restrict the incident light linearly polarized along [110] (or $[\bar{1}10]$) direction, we can find $j_{x'}^{y'}$ and $j_{y'}^{x'}$ are

the only nonzero PSCs regardless the interplay of SIA and BIA. The spectrums of $j_{x'}^{y'}$ and $j_{y'}^{x'}$ induced by [110]-linearly-polarized light for HgTe QWs with different well widths are displayed in Fig. 6(c) and 6(d). We can see the spectrums of $j_{x'}^{y'}$ and $j_{y'}^{x'}$ show sharp peaks near the optical absorption edges. At photon energies above the absorption edges, the PSCs decrease quickly. The reason for the PSCs' decreasing is due to the band mixing at large \mathbf{k} greatly suppresses the expectation values of spins. In addition, we find the band mixing effect is more prominent for $j_{x'}^{y'}$ than $j_{y'}^{x'}$ in the case of [110]-linearly-polarized light. Therefore the magnitudes of $j_{x'}^{y'}$ are generally smaller than that of $j_{y'}^{x'}$. Interestingly, we find $j_{y'}^{x'}$ change signs if one increase L_w across the critical thickness 5.9 nm. Or in other words, $j_{y'}^{x'}$ have different signs for HgTe QWs with normal phase and inverted phase. This is because the contributions of E1 and H1 states to $j_{y'}^{x'}$ change signs if the order of E1 and H1 is reversed. This feature implies $j_{y'}^{x'}$ might be utilized to characterize the quantum phase of HgTe QWs. In contrast, $j_{x'}^{y'}$ is not so sensitive to the energy order of subbands, mostly because of the strong band mixing effect.

VI. CONCLUSION

In summary, we present a theoretical method for the calculations of circular photogalvanic charge currents and linearly photogalvanic pure spin currents based on the eight-band $\mathbf{k} \cdot \mathbf{p}$ model and density matrix formalism. This method could take full account of the complex band structure details and different type of inversion asymmetries, therefore is used to investigate the CPGE currents, PSCs and their microscopic origins in HgTe QWs with different quantum phases. Our calculations show CPGE could be remarkably enhanced at certain range of energy spectrum due to the distorted band structures of heavily inverted HgTe QWs. The interference of RSOI and DSOI could lead to the CPGE currents show anisotropy behaviors about the azimuth angle of oblique incident light. The spectrums of γ_{xx} and γ_{yx} are very complicated for QWs with abnormal band structures, so that γ_{yx}/γ_{xx} is not always equal to the RD ratio. For [110]-linearly-polarized light at normal incidence, the light could drive two nonzero PSCs, i.e., $j_{x'}^{y'}$ and $j_{y'}^{x'}$ ($x' \parallel [110]$ and $y' \parallel [\bar{1}10]$), respectively. We find $j_{y'}^{x'}$ are different in signs

for HgTe QWs with normal phase and inverted phase. These findings are helpful for understanding the experimental results and can be taken advantages in HgTe-based infrared/terahertz optoelectronic devices.

ACKNOWLEDGMENTS

This work was supported by the National Natural Science Foundation of China (Grant No. 11104232), the Fundamental Research Funds for the Central Universities (Grant No. 20720160019), and the Natural Science Foundation of Fujian Province of China (Grant No. 2016J05163). Jiang-Tao Liu was supported by the National Natural Science Foundation of China (Grant No. 11364033).

Appendix A: Eight-Band Hamiltonian

The band structure of narrow gap QWs can be well described within the framework of Burt's envelope function formalism together with Kane's eight-band $\mathbf{k} \cdot \mathbf{p}$ Hamiltonian [27]. The exact form of Hamiltonian is dependent on the choice of basis set. In this work, the eight-band basis set is chosen as

$$\begin{aligned}
 \phi_1 &= \left| \frac{1}{2}, \frac{1}{2} \right\rangle = |S \uparrow\rangle, \\
 \phi_2 &= \left| \frac{1}{2}, -\frac{1}{2} \right\rangle = |S \downarrow\rangle, \\
 \phi_3 &= \left| \frac{3}{2}, \frac{3}{2} \right\rangle = \frac{1}{\sqrt{2}} |(X + iY) \uparrow\rangle, \\
 \phi_4 &= \left| \frac{3}{2}, \frac{1}{2} \right\rangle = \frac{i}{\sqrt{6}} |(X + iY) \downarrow - 2Z \uparrow\rangle, \\
 \phi_5 &= \left| \frac{3}{2}, -\frac{1}{2} \right\rangle = \frac{1}{\sqrt{6}} |(X - iY) \uparrow + 2Z \downarrow\rangle, \\
 \phi_6 &= \left| \frac{3}{2}, -\frac{3}{2} \right\rangle = \frac{i}{\sqrt{2}} |X - iY \downarrow\rangle, \\
 \phi_7 &= \left| \frac{1}{2}, \frac{1}{2} \right\rangle = \frac{1}{\sqrt{3}} |(X + iY) \downarrow + Z \uparrow\rangle, \\
 \phi_8 &= \left| \frac{1}{2}, -\frac{1}{2} \right\rangle = -\frac{i}{\sqrt{3}} |(X - iY) \uparrow - Z \downarrow\rangle, \quad (\text{A1})
 \end{aligned}$$

In the presentation of this basis set, the eight-band Hamiltonian \hat{H}_K is

TABLE I. The band parameters used in our calculations. These parameters are taken from from Ref. 27 and 47.

	E_v (eV)	E_g (eV)	$E_p = 2m_0P_0^2/\hbar^2$ (eV)	Δ (eV)	F	γ_1	γ_2	γ_3	κ	n_r
HgTe [27]	0	-0.303	18.8	1.08	0	4.1	0.5	0.3	-0.4	3.28
Hg _{0.3} Cd _{0.7} Te [47]	-0.399	1.006	18.8	1.0	-0.8	3.3	0.1	0.9	-0.8	3.28

$$\begin{bmatrix}
 \mathcal{A} & 0 & i\sqrt{3}\mathcal{V}^\dagger & \sqrt{2}\mathcal{U} & i\mathcal{V} & 0 & i\mathcal{U} & \sqrt{2}\mathcal{V} \\
 0 & \mathcal{A} & 0 & -\mathcal{V}^\dagger & i\sqrt{2}\mathcal{U} & -\sqrt{3}\mathcal{V} & i\sqrt{2}\mathcal{V}^\dagger & -\mathcal{U} \\
 -i\sqrt{3}\mathcal{V} & 0 & -(\mathcal{P} + \mathcal{Q}) & \mathcal{L} - i\sqrt{3}\mathcal{N} & \mathcal{M} & 0 & \frac{i}{\sqrt{2}}\mathcal{L} + \sqrt{\frac{3}{2}}\mathcal{N} & -i\sqrt{2}\mathcal{M} \\
 \sqrt{2}\mathcal{U} & -\mathcal{V} & \mathcal{L}^\dagger - i\sqrt{3}\mathcal{N}^\dagger & -(\mathcal{P} - \mathcal{Q}) & -2i\mathcal{N} & \mathcal{M} & i\sqrt{2}\mathcal{Q} & i\sqrt{\frac{3}{2}}\mathcal{L} - \sqrt{\frac{1}{2}}\mathcal{N} \\
 -i\mathcal{V}^\dagger & -i\sqrt{2}\mathcal{U} & \mathcal{M}^\dagger & 2i\mathcal{N}^\dagger & -(\mathcal{P} - \mathcal{Q}) & -\mathcal{L} - i\sqrt{3}\mathcal{N} & -i\sqrt{\frac{3}{2}}\mathcal{L}^\dagger + \sqrt{\frac{1}{2}}\mathcal{N}^\dagger & i\sqrt{2}\mathcal{Q} \\
 0 & -\sqrt{3}\mathcal{V}^\dagger & 0 & \mathcal{M}^\dagger & -\mathcal{L}^\dagger + i\sqrt{3}\mathcal{N}^\dagger & -(\mathcal{P} + \mathcal{Q}) & -i\sqrt{2}\mathcal{M}^\dagger & -\frac{i}{\sqrt{2}}\mathcal{L}^\dagger - \sqrt{\frac{3}{2}}\mathcal{N}^\dagger \\
 -i\mathcal{U} & -i\sqrt{2}\mathcal{V} & -\frac{i}{\sqrt{2}}\mathcal{L}^\dagger + \sqrt{\frac{3}{2}}\mathcal{N}^\dagger & -i\sqrt{2}\mathcal{Q} & i\sqrt{\frac{3}{2}}\mathcal{L} - \sqrt{\frac{1}{2}}\mathcal{N}^\dagger & i\sqrt{2}\mathcal{M} & -\mathcal{P} - \Delta & 2i\mathcal{N} \\
 \sqrt{2}\mathcal{V}^\dagger & -\mathcal{U} & i\sqrt{2}\mathcal{M}^\dagger & -i\sqrt{\frac{3}{2}}\mathcal{L}^\dagger - \sqrt{\frac{1}{2}}\mathcal{N}^\dagger & -i\sqrt{2}\mathcal{Q} & \frac{i}{\sqrt{2}}\mathcal{L} - \sqrt{\frac{3}{2}}\mathcal{N} & -2i\mathcal{N}^\dagger & -\mathcal{P} - \Delta
 \end{bmatrix} \quad (\text{A2})$$

where

$$\begin{aligned}
 \mathcal{A} &= E_v + E_g + \frac{\hbar^2}{2m_0}[(2F + 1)k^2 + \hat{k}_z(2F + 1)\hat{k}_z], \\
 \mathcal{P} &= -E_v + \frac{\hbar^2}{2m_0}(\gamma_1 k^2 + \hat{k}_z \gamma_1 \hat{k}_z), \\
 \mathcal{Q} &= \frac{\hbar^2}{2m_0}(\gamma_2 k^2 - 2\hat{k}_z \gamma_2 \hat{k}_z), \\
 \mathcal{L} &= i \frac{2\sqrt{3}\hbar^2}{m_0} k_- \{\gamma_3, \hat{k}_z\}, \\
 \mathcal{M} &= -\frac{\sqrt{3}\hbar^2}{2m_0} [\gamma_2 (k_x^2 - k_y^2) - i2\gamma_3 k_x k_y], \\
 \mathcal{N} &= \frac{\hbar^2}{2m_0} k_- [\hat{k}_z, \kappa], \\
 \mathcal{U} &= \frac{1}{\sqrt{3}} P_0 \hat{k}_z, \\
 \mathcal{V} &= \frac{1}{\sqrt{6}} P_0 k_-. \quad (\text{A3})
 \end{aligned}$$

For the (001)-oriented HgTe QW, \hat{k}_z should be replaced by $\hat{k}_z \rightarrow -i\partial/\partial z$ as a result of quantum confinement. $\{\hat{A}, \hat{B}\} = (\hat{A}\hat{B} + \hat{B}\hat{A})/2$ and $[\hat{A}, \hat{B}] = \hat{A}\hat{B} - \hat{B}\hat{A}$ denote the anticommutator and usual commutator for operators \hat{A} and \hat{B} . $\mathbf{k} \equiv (k_x, k_y)$ is the in-plane wave vector, $k^2 \equiv k_x^2 + k_y^2$ and $k_\pm \equiv k_x \pm ik_y$. The band structure parameters, including E_v , E_g , P_0 , F , γ_1 , γ_2 , γ_3 and κ are dependent on the materials of each layers. These parameters for HgTe and Hg_{0.3}Cd_{0.7}Te are listed in Table I. In the Hamiltonian of heterostructures, the parameters can be assumed as the step functions along growth direction z . In our calculation, \hat{H}_K is taken as the Hamiltonian of symmetric HgTe QW, which means the step functions of parameters have mirror reflection symmetry. As a consequence, \hat{H}_K holds the spacial inversion symmetry, so it does not give rise to the spin-splitting of band structure.

For a general HgTe QW with Hamiltonian \hat{H}_0 , the eigenenergy and the eigenstate of electron with wave vector \mathbf{k} can be obtained by solving the time-independent Schrödinger equation

$$\hat{H}_0 |m, \mathbf{k}\rangle = \varepsilon_m(\mathbf{k}) |m, \mathbf{k}\rangle. \quad (\text{A4})$$

Here m is the subband index, $\varepsilon_m(\mathbf{k})$ is the eigenenergy, and $|m, \mathbf{k}\rangle$ is the eigenstate. $|m, \mathbf{k}\rangle$ is a vector with eight components of envelope functions $|m, \mathbf{k}\rangle = \exp(i\mathbf{k} \cdot \mathbf{r}) [\varphi_1^m(z), \varphi_2^m(z), \dots, \varphi_8^m(z)]^T$. Eq. (A4) is equivalent to a system of coupled differential equations, which can be solved by the plane wave expansion method, i.e., one can expand each envelope function $\varphi_n^m(z)$ as a series of plane waves

$$\varphi_n^m(z) = \frac{1}{\sqrt{L}} \sum_{j=-N}^N c_{nj}^m \exp(ik_j z), \quad (\text{A5})$$

where $k_j = 2j\pi/L$ and L is the total length of the structure, N is the cut-off plane wave number. By moderately choosing N ($N = 40$ is used in this work), one can avoid the spurious solutions [48] as well as getting results with required accuracy. Substituting Eq.(A5) into Eq.(A4), the coupled differential equations is then converted to the standard eigenvalue problem which can be numerically solved by matrix diagonalization.

Appendix B: Bulk Inversion Asymmetry terms

For the eight-band model, there are two kinds of terms which could give birth to BIA, i.e., terms weighted by B_{8v}^\pm, B_{7v}^\pm [32, 33] and C_k [34, 35], respectively. The terms with B_{8v}^\pm (B_{7v}^\pm) come from the indirect coupling between Γ_6 and Γ_8 (Γ_7) bands mediated by the remote bands. These terms are quadratic in \mathbf{k} , and appear in the off-diagonal blocks of Hamiltonian. The terms with C_k are

TABLE II. The BIA parameters used in our calculations. These parameters are obtained from in Ref. 32, 34, and 49.

	B_+ (eV·Å ²)	B_- (eV·Å ²)	C_k (eV·Å)
HgTe	-20.0	1.0	-0.0746
CdTe	-21.44	-0.635	-0.0234

^a The BIA parameters for Hg_xCd_{1-x}Te are assumed to be the linear interpolation of the parameters of HgTe and CdTe.

linear in \mathbf{k} and present in the Γ_8 block of Hamiltonian (called Γ_8 band \mathbf{k} -linear terms). They mainly come from the second-order perturbation terms combing the matrix elements of $\mathbf{k} \cdot \mathbf{p}$ and the spin-orbit operator \hat{H}_{SO} . The values of B_{8v}^\pm, B_{7v} can be evaluated from 14-band Hamiltonian of the extended Kane model [32], and the values of C_k have been studied by Cardona et al. [34]. Here, for Hg_{1-x}Cd_xTe, we neglect the difference between B_{8v}^+ and B_{7v} , and assume $B_+ \simeq (B_{8v}^+ + B_{7v})/2$, $B_- = B_{8v}^-$. These BIA parameters are presented in Table II.

In the representation of eight-band basis [Eq. (A1)], the form of \hat{H}_{BIA} is

$$\hat{H}_{BIA} = \begin{pmatrix} 0 & 0 & i\sqrt{3}\mathcal{W}_2^\dagger & -\sqrt{2}(\mathcal{W}_1 + \mathcal{T}_1) & -i\mathcal{W}_2 & \mathcal{T}_2 & -i\mathcal{W}_1 & -\sqrt{2}\mathcal{W}_2 \\ 0 & 0 & -i\mathcal{T}_2 & -\mathcal{W}_2^\dagger & -i\sqrt{2}(\mathcal{W}_1 - \mathcal{T}_1) & \sqrt{3}\mathcal{W}_2 & i\sqrt{2}\mathcal{W}_2^\dagger & \mathcal{W}_1 \\ -i\sqrt{3}\mathcal{W}_2 & i\mathcal{T}_2^\dagger & 0 & \mathcal{C}_1 & 2\mathcal{C}_2 & \sqrt{3}\mathcal{C}_1^\dagger & \frac{i}{\sqrt{2}}\mathcal{C}_1 & i\sqrt{2}\mathcal{C}_2 \\ -\sqrt{2}(\mathcal{W}_1^\dagger + \mathcal{T}_1^\dagger) & -\mathcal{W}_2 & \mathcal{C}_1^\dagger & 0 & -\sqrt{3}\mathcal{C}_1 & -2\mathcal{C}_2 & 0 & i\sqrt{\frac{3}{2}}\mathcal{C}_1 \\ i\mathcal{W}_2^\dagger & i\sqrt{2}(\mathcal{W}_1^\dagger - \mathcal{T}_1^\dagger) & 2\mathcal{C}_2^\dagger & -\sqrt{3}\mathcal{C}_1^\dagger & 0 & \mathcal{C}_1 & i\sqrt{\frac{3}{2}}\mathcal{C}_1^\dagger & 0 \\ \mathcal{T}_2^\dagger & \sqrt{3}\mathcal{W}_2^\dagger & \sqrt{3}\mathcal{C}_1 & -2\mathcal{C}_2^\dagger & \mathcal{C}_1^\dagger & 0 & -i\sqrt{2}\mathcal{C}_2 & \frac{i}{\sqrt{2}}\mathcal{C}_1^\dagger \\ i\mathcal{W}_1^\dagger & -i\sqrt{2}\mathcal{W}_2 & -\frac{i}{\sqrt{2}}\mathcal{C}_1^\dagger & 0 & -i\sqrt{\frac{3}{2}}\mathcal{C}_1 & i\sqrt{2}\mathcal{C}_2^\dagger & 0 & 0 \\ -\sqrt{2}\mathcal{W}_2^\dagger & \mathcal{W}_1^\dagger & -i\sqrt{2}\mathcal{C}_2^\dagger & -i\sqrt{\frac{3}{2}}\mathcal{C}_1^\dagger & 0 & -\frac{i}{\sqrt{2}}\mathcal{C}_1 & 0 & 0 \end{pmatrix} \quad (\text{B1})$$

where

$$\begin{aligned} \mathcal{W}_1 &= -\frac{i}{\sqrt{3}}B_+k_xk_y, \\ \mathcal{W}_2 &= -\frac{1}{\sqrt{6}}k_+\{B_+, \hat{k}_z\}, \\ \mathcal{T}_1 &= -\frac{1}{2\sqrt{3}}B_-(k_x^2 - k_y^2), \\ \mathcal{T}_2 &= -\frac{1}{3\sqrt{2}}[B_-(k_x^2 + k_y^2) - \hat{k}_zB_-\hat{k}_z], \\ \mathcal{C}_1 &= -\frac{1}{2}iC_kk_+, \\ \mathcal{C}_2 &= -\frac{1}{2}\{C_k, \hat{k}_z\}. \end{aligned} \quad (\text{B2})$$

In the elements of \hat{H}_{BIA} , \hat{k}_z is also replaced by $\hat{k}_z \rightarrow -i\partial/\partial_z$ as in Eq. (A3). \hat{H}_{BIA} could give a small modification of \hat{H}_K , and can be included in \hat{H}_0 and together solved by Eq. (A4).

Appendix C: Effective Magnetic Field of Spin-Orbit Interactions

The spin-orbit coupling originates from the relativistic transformation of electric field and magnetic field. In the reference frame of a moving electron, a static electric field

is transformed into a magnetic field depending on the velocity (or the wave vector \mathbf{k}) of electron. The electron spin could couple to this transformed effective magnetic field via the magnetic dipole interaction. Therefore in this sense, the effects of SOI can be directly by analogy with a \mathbf{k} -dependent effective magnetic field $\mathfrak{B}(\mathbf{k})$. Similar to the Zeeman effect of a real magnetic field, the effective magnetic field of SOI could also split the energy band into two branches, with the spin orientation of the upper (lower) branch parallel (antiparallel) to the direction of $\mathfrak{B}(\mathbf{k})$. In different bands, electron may feel SOI with different strengths. Therefore we should label the effective magnetic field of SOI felt by electron in n-th subband with wave vector \mathbf{k} as $\mathfrak{B}_n(\mathbf{k})$. The SOI-induced spin-splitting and electron spin orientations will be closely dependent on the magnitudes and directions of $\mathfrak{B}_n(\mathbf{k})$ respectively. Due to $\mathfrak{B}_n(\mathbf{k})$ changes with \mathbf{k} , the spin-splitting and spin orientations change as well, producing the spin texture of n-th subband in \mathbf{k} space.

The effective magnetic field can be defined by attributing the spin-splitting of SOI to the Zeeman effect of $\mathfrak{B}_n(\mathbf{k})$. In the eight-band basis, the Zeeman terms write as [32]

$$\hat{H}_z = \mu_B \mathbf{B} \cdot \hat{\Sigma}, \quad (\text{C1})$$

where μ_B is the Bohr magneton, \mathbf{B} is the external magnetic field, and $\hat{\Sigma} = (\hat{\Sigma}_x, \hat{\Sigma}_y, \hat{\Sigma}_z)$ is the vector of eight-band spin matrices [50]. $\hat{\Sigma}$ can be obtained by

$\hat{\Sigma} = \sigma \otimes \mathbb{L}_{orb}$, where $\sigma = (\sigma_x, \sigma_y, \sigma_z)$ is the vector of Pauli spin matrices, and \mathbb{L}_{orb} refers to the orbital part of the basis function (A1). The form of $\hat{\Sigma}$ can be found in Ref. 46. Let $\mathfrak{B}_n(\mathbf{k}) = \mathbf{B}$, we can obtain

$$\Delta\varepsilon_n(\mathbf{k}) = \varepsilon_{n+}(\mathbf{k}) - \varepsilon_{n-}(\mathbf{k}) \approx \mu_B \mathfrak{B}_n(\mathbf{k}) \cdot \Sigma_n(\mathbf{k}). \quad (\text{C2})$$

$\varepsilon_{n\pm}(\mathbf{k})$ are the energies for the upper (lower) branch of the n -th subband and $\Delta\varepsilon_n(\mathbf{k})$ is the spin-splitting. $\Sigma_n(\mathbf{k}) \equiv \langle n+, \mathbf{k} | \hat{\Sigma} | n+, \mathbf{k} \rangle - \langle n-, \mathbf{k} | \hat{\Sigma} | n-, \mathbf{k} \rangle$, and $|n\pm, \mathbf{k}\rangle$ are the eigenstates for the upper (lower) branch of the n -th subband. Using Eq. (C2), we can get the expression

for the effective magnetic field of n -th subband

$$\mathfrak{B}_n(\mathbf{k}) = \mu_B \Delta\varepsilon_s(\mathbf{k}) \frac{\Sigma_n(\mathbf{k})}{|\Sigma_n(\mathbf{k})|}. \quad (\text{C3})$$

Eq. (C3) indicates that the magnitudes and directions of $\mathfrak{B}_n(\mathbf{k})$ could represent the spin-splitting and spin orientations (or spin texture) of n -th subband, respectively. For the analysis of SOI-induced phenomena, it is very helpful to visualize the \mathbf{k} space distributions of effective magnetic fields.

-
- [1] A. Rogalski, Rep. Prog. Phys. **68**, 2267 (2005).
[2] X. C. Zhang, A. Pfeuffer-Jeschke, K. Ortner, V. Hock, H. Buhmann, C. R. Becker, and G. Landwehr, Phys. Rev. B **63**, 245305 (2001).
[3] Y. S. Gui, C. R. Becker, N. Dai, J. Liu, Z. J. Qiu, E. G. Novik, M. Schafer, X. Z. Shu, J. H. Chu, H. Buhmann, and L. W. Molenkamp, Phys. Rev. B **70**, 115328 (2004).
[4] W. Yang and K. Chang, Phys. Rev. B **74**, 193314 (2006).
[5] X. Z. Liu, G. Yu, L. M. Wei, T. Lin, Y. G. Xu, J. R. Yang, Y. F. Wei, S. L. Guo, J. H. Chu, N. L. Rowell, and D. J. Lockwood, J. Appl. Phys. **113**, 013704 (2013).
[6] X. C. Zhang, K. Ortner, A. Pfeuffer-Jeschke, C. R. Becker, and G. Landwehr, Phys. Rev. B **69**, 115340 (2004).
[7] W. Yang, K. Chang, and S.-C. Zhang, Phys. Rev. Lett. **100**, 056602 (2008).
[8] C. Brune, A. Roth, E. G. Novik, M. König, H. Buhmann, E. M. Hankiewicz, W. Hanke, J. Sinova, and L. W. Molenkamp, Nat Phys **6**, 448 (2010).
[9] B. A. Bernevig, T. L. Hughes, and S.-C. Zhang, Science **314**, 1757 (2006).
[10] M. König, S. Wiedmann, C. Brune, A. Roth, H. Buhmann, L. W. Molenkamp, X.-L. Qi, and S.-C. Zhang, Science **318**, 766 (2007).
[11] D. Pesin and A. H. MacDonald, Nat Mater **11**, 409 (2012).
[12] X.-L. Qi and S.-C. Zhang, Rev. Mod. Phys. **83**, 1057 (2011).
[13] S. D. Ganichev, W. Weber, J. Kiermaier, S. N. Danilov, P. Olbrich, D. Schuh, W. Wegscheider, D. Bougeard, G. Abstreiter, and W. Prettl, J. Appl. Phys. **103**, 114504 (2008).
[14] S. N. Danilov, B. Wittmann, P. Olbrich, W. Eder, W. Prettl, L. E. Golub, E. V. Beregulin, Z. D. Kvon, N. N. Mikhailov, S. A. Dvoretzky, V. A. Shalygin, N. Q. Vinh, A. F. G. van der Meer, B. Murdin, and S. D. Ganichev, J. Appl. Phys. **105**, 013106 (2009).
[15] E. L. Ivchenko and G. E. Pikus, in *Superlattices and Other Heterostructures: Symmetry and Optics* (Springer Berlin Heidelberg, Berlin, Heidelberg, 1997) pp. 305–338.
[16] S. D. Ganichev, E. L. Ivchenko, S. N. Danilov, J. Eroms, W. Wegscheider, D. Weiss, and W. Prettl, Phys. Rev. Lett. **86**, 4358 (2001).
[17] S. D. Ganichev and W. Prettl, J. Phys.: Condens. Matter **15**, R935 (2003).
[18] É. I. Rashba, Sov. Phys. Solid State **2**, 1109 (1960).
[19] G. Dresselhaus, Phys. Rev. **100**, 580 (1955).
[20] L. E. Golub, Phys. Rev. B **67**, 235320 (2003).
[21] S. D. Ganichev, V. V. Bel'kov, L. E. Golub, E. L. Ivchenko, P. Schneider, S. Giglberger, J. Eroms, J. De Boeck, G. Borghs, W. Wegscheider, D. Weiss, and W. Prettl, Phys. Rev. Lett. **92**, 256601 (2004).
[22] S. Giglberger, L. E. Golub, V. V. Bel'kov, S. N. Danilov, D. Schuh, C. Gerl, F. Rohlffing, J. Stahl, W. Wegscheider, D. Weiss, W. Prettl, and S. D. Ganichev, Phys. Rev. B **75**, 035327 (2007).
[23] B. Wittmann, S. N. Danilov, V. V. Bel'kov, S. A. Tarasenko, E. G. Novik, H. Buhmann, C. Brune, L. W. Molenkamp, Z. D. Kvon, N. N. Mikhailov, S. A. Dvoretzky, N. Q. Vinh, A. F. G. v. d. Meer, B. Murdin, and S. D. Ganichev, Semicond. Sci. Technol. **25**, 095005 (2010).
[24] P. Olbrich, C. Zoth, P. Vierling, K. M. Dantscher, G. V. Budkin, S. A. Tarasenko, V. V. Bel'kov, D. A. Kozlov, Z. D. Kvon, N. N. Mikhailov, S. A. Dvoretzky, and S. D. Ganichev, Phys. Rev. B **87**, 235439 (2013).
[25] B. Zhou and S.-Q. Shen, Phys. Rev. B **75**, 045339 (2007).
[26] K. Ortner, X. C. Zhang, A. Pfeuffer-Jeschke, C. R. Becker, G. Landwehr, and L. W. Molenkamp, Phys. Rev. B **66**, 075322 (2002).
[27] E. G. Novik, A. Pfeuffer-Jeschke, T. Jungwirth, V. Latussek, C. R. Becker, G. Landwehr, H. Buhmann, and L. W. Molenkamp, Phys. Rev. B **72**, 035321 (2005).
[28] J. Li and K. Chang, Appl. Phys. Lett. **95**, 222110 (2009).
[29] B. Buttner, C. X. Liu, G. Tkachov, E. G. Novik, C. Brune, H. Buhmann, E. M. Hankiewicz, P. Recher, B. Trauzettel, S. C. Zhang, and L. W. Molenkamp, Nat. Phys. **7**, 418 (2011).
[30] R. W. Boyd, in *Nonlinear Optics (Third Edition)* (Academic Press, Burlington, 2008) pp. 135–206.
[31] C. F. Klingshirn, in *Semiconductor Optics* (Springer Berlin Heidelberg, Berlin, Heidelberg, 2012) pp. 623–700.
[32] R. Winkler, *Spin-Orbit Coupling Effects in Two-Dimensional Electronic Structures* (Springer Berlin Heidelberg, Berlin, Heidelberg, 2003).
[33] E. O. Kane, in *Semiconductor and Semimetals*, Vol. 1, edited by R. K. Willardson and A. C. Beer (Academic, New York, 1966) p. 75.
[34] M. Cardona, N. E. Christensen, and G. Fasol, Phys. Rev. Lett. **56**, 2831 (1986).
[35] M. Cardona, N. E. Christensen, and G. Fasol,

- Phys. Rev. B **38**, 1806 (1988).
- [36] H. R. Trebin, U. Rössler, and R. Ranvaud, Phys. Rev. B **20**, 686 (1979).
- [37] W. Knap, C. Skierbiszewski, A. Zduniak, E. Litwin-Staszewska, D. Bertho, F. Kobbi, J. L. Robert, G. E. Pikus, F. G. Pikus, S. V. Iordanskii, V. Mosser, K. Zekentes, and Y. B. Lyanda-Geller, Phys. Rev. B **53**, 3912 (1996).
- [38] N. S. Averkiev, M. M. Glazov, and S. A. Tarasenko, Solid State Commun. **133**, 543 (2005).
- [39] N. S. Averkiev and L. E. Golub, Phys. Rev. B **60**, 15582 (1999).
- [40] B. A. Bernevig, J. Orenstein, and S.-C. Zhang, Phys. Rev. Lett. **97**, 236601 (2006).
- [41] J. D. Koralek, C. P. Weber, J. Orenstein, B. A. Bernevig, S.-C. Zhang, S. Mack, and D. D. Awschalom, Nature **458**, 610 (2009).
- [42] C. Yin, B. Shen, Q. Zhang, F. Xu, N. Tang, L. Cen, X. Wang, Y. Chen, and J. Yu, Appl. Phys. Lett. **97**, 181904 (2010).
- [43] C. Jiang, Y. Chen, H. Ma, J. Yu, and Y. Liu, Appl. Phys. Lett. **98**, 232116 (2011).
- [44] R. D. R. Bhat, F. Nastos, A. Najmaie, and J. E. Sipe, Phys. Rev. Lett. **94**, 096603 (2005).
- [45] S. A. Tarasenko and E. L. Ivchenko, JETP Lett. **81**, 231.
- [46] J. Li, W. Yang, and K. Chang, Phys. Rev. B **80**, 035303 (2009).
- [47] O. Madelung, U. Rössler, and M. Schulz, eds., in *II-VI and I-VII Compounds; Semimagnetic Compounds* (Springer Berlin Heidelberg, Berlin, Heidelberg, 1999) pp. 1–18.
- [48] W. Yang and K. Chang, Phys. Rev. B **72**, 233309 (2005).
- [49] R. Winkler, L. Y. Wang, Y. H. Lin, and C. S. Chu, Solid State Commun. **152**, 2096 (2012).
- [50] For materials in a real magnetic field, the eight-band spin matrices in Zeeman terms should contain the effective g factor parameter κ . However, we find the difference with and without κ are small. Besides, we are actually interested in the relative magnitude of effective magnetic field, so the terms with κ is neglected here.